Application of SPS in the fabrication of UN and (U,Th)N pellets from microspheres

Journal of Nuclear Materials 536 (2020) 152181

Contents lists available at ScienceDirect

Journal of Nuclear Materials

journal homepage: www.elsevier.com/locate/jnucmat

Application of SPS in the fabrication of UN and (U,Th)N pellets from microspheres

L.G. Gonzalez Fonseca [a, *], M. Hedberg [a], L. Huan [b], P. Olsson [b], T. Retegan Vollmer [a]

[a] Division of Nuclear Chemistry, Department of Chemistry and Chemical Engineering, Chalmers University of Technology, 412 96, Gothenburg, Sweden
[b] Royal Institute of Technology, KTH, Stockholm, Sweden

HIGHLIGHTS

- Homogeneous thorium nitride and uranium nitride solid solution was achieved.
- Densities exceeding 90% of theoretical density were measured in produced pellets.
- Influence of thorium content on sintering onset temperatures during SPS was observed.
- No blackberry structure was retained in the produced pellets using SPS.
- Low porosity observed at temperatures of 1550 °C and above.

ARTICLE INFO

Article history:
Received 28 February 2020
Received in revised form
15 April 2020
Accepted 15 April 2020
Available online 30 April 2020

Keywords:
Uranium nitride
Microspheres
Internal gelation
Doping
Sintering
SPS
Theoretical density
Porosity

ABSTRACT

In this study, the process involved in the fabrication of a potential accident tolerant fuel is described. Homogeneous uranium nitride microspheres doped with different thorium content were successfully manufactured using an internal gelation process followed by carbothermic reduction, and nitridation. Elemental analysis of the materials showed low carbon and oxygen content, the two major impurities found in the products of carbothermic reduction. Uranium nitride microspheres were pressed and sintered using spark plasma sintering (SPS) to produce pellets with variable density. Final density can be tailored by choosing the sintering temperature, pressure and time. Density values of 77–98% of theoretical density (%TD) were found. As expected, higher temperatures and pressures resulted in a denser material. Furthermore, a direct correlation between the onset sintering temperature and thorium content in the materials was observed. The change of onset temperature has been related to an increment in the activation energy for self-diffusion due to the substitution of uranium atoms by thorium in the crystal structure.

1. Introduction

After Fukushima Daiichi nuclear accident, international efforts have been focused on manufacturing fuels that can withstand accident conditions for an extended period of time. Such fuel concepts are known as Accident Tolerant Fuels (ATF). These materials must exhibit the same or improved properties compared to current fuels while reducing oxidation kinetics and hydrogen production rates under accident conditions [1,2]. In order to accomplish this, either the cladding, the fuel or both must be modified. Several developed concepts are focused on changing the cladding material, as this is the physical barrier between the coolant and the fuel [3]. However, such modification will cause neutron penalties in the fuel, and therefore the uranium density in the fuel must be increased to maintain the fuel efficiency. Uranium carbide (UC), uranium mononitride (UN) and uranium silicide (U_3Si_2) are examples of modified fuel candidates for ATF [4]. Uranium nitride has been previously used in the sodium-cooled BR-10 reactor, nearly 20 years ago, and therefore its chemical and physical characteristics are well known [5]. The properties of some potential future fuel materials are summarized in Table 1 and compared to UO_2. As can be seen, the thermal conductivity of all these alternative materials increases with temperature, in contrast to UO_2. This feature considerably reduces the pellet's centerline temperature at normal and accident

* Corresponding author.
E-mail address: luisg@chalmers.se (L.G. Gonzalez Fonseca).

https://doi.org/10.1016/j.jnucmat.2020.152181

Table 1
Physical and thermal properties of uranium-based accident tolerant fuels (ATF).

Fuel	Thermal conductivity (W/mK: 600–1400K)	Melting point (K)	Peak centerline temperature (K)	Density (g/cm^3)	**Uranium density in the compound (g/cm^3)** [8]
UO_2	6–2.5 [8]	3148 [9]	2800 [10],[a]	10.96 [9]	9.7 [9]
UC	12.6–16 [11]	2768 [12]	900-1300 [11]	13.63 [12]	13.0 [9]
UN	19-25 [13]	2903 [9]	1200 [10],[a]	14.32 [9]	13.5 [9]
U_3Si_2	15–27.5 [14]	1938 [9]	–	12.2 [14]	11.3 [14]

[a] Modelled centerline temperature at beginning of life (BOL).

conditions [6,7]. Moreover, uranium density in UN, U_3Si_2, and UC is higher compared to UO_2, which could allow an extended fuel cycle length or reduction of the otherwise required enrichment.

These fuels are not optimal either, as they present some drawbacks that are not shown by UO_2. For example, uranium nitride reacts in an oxygen environment to form UO_2, or U_3O_8, releasing nitrogen as a byproduct, as seen in Eq. *1* and *2* [15,16].

$$UN(s) + \frac{4}{3}O_2(g) \rightarrow \frac{1}{3}U_3O_8(s) + \frac{1}{2}N_2(g) \quad (1)$$

$$2UN(s) + 2O_2(g) \rightarrow 2UO_2(s) + 2N_2(g) \quad (2)$$

If water is present, ammonia and hydrogen are produced instead, as observed in Eq. *3* [17] and *4* [18]. Production of UN fuels should thus be performed in an oxygen and moisture-free atmosphere, adding increased complexity to the fabrication process.

$$2UN(s) + 4H_2O \rightarrow 2UO_2(s) + 2NH_3(aq) + H_2(g) \quad (3)$$

$$3UN(s) + 8H_2O \rightarrow U_3O_8(s) + 3NH_3(aq) + 3.5H_2(g) \quad (4)$$

Oxidation of UN takes place at different temperatures depending on the surface area available for the reaction [19]. For example, fine powders of UN will oxidize in air or water at ambient temperature (20 °C), while non-porous pellets can withstand temperatures up to 100 °C [18,20]. By the end of 2018, 96% of the power-producing nuclear reactors in the world were water-cooled reactors (BWR, PWR, PHWR, LWGR), which makes the industrial implementation of nitride fuels a challenge [21].

Different methods to improve the corrosion resistance of UN have been discussed before. One of these is doping with additives such as chromium, aluminum, and other metals that are known for forming protective oxide layers in various types of corrosion resistance applications [22,23]. Such protective oxide layer would be able to reduce the fuel oxidation rate by limiting the interaction between the UN and the oxidation agent (in this case water or steam). The selection of an appropriate element must consider various features, such as neutron absorption penalties or capability to form solid solutions with the uranium nitride. Addition of thorium was proposed in this work due to the likely formation of a solid solution between U and Th in the nitride phase, and the possible development of a protective thoria layer on the surface, which could slow down the oxidation of uranium nitride [24].

The high resistance of uranium nitrides to sintering has proven to be an inconvenience in obtaining materials with densities higher than 90% of theoretical density [25]. Conventionally, the sintering of UN requires temperatures of 2300 °C to yield densities of 95% of theoretical density [26]. More recently, Bauer et al. [27] were able to reduce this sintering temperature to 1900 °C by using UN powder with smaller particle sizes of 2–10 μm. Other methods have been developed to try to further reduce the sintering temperature, such as liquid phase sintering and electric current-assisted sintering [28]. Amongst these, spark plasma sintering (SPS) has proven to be able to achieve UN densities higher than 90% TD in less than 5 min using high purity UN powder at 1650 °C [29]. However, the use of fine radioactive powder is undesirable due to the possibility of spreading contamination in the production process. One method used to solve this inconvenience is the synthesis of uranium oxides, carbides, and nitrides in the shape of spheres with approx. 500–1000 μm diameter [30]. Different methods have been developed to produce microspheres, such as the ORNL process [31], the external gelation process [32], and the internal gelation process [33], all of which start with an aqueous solution as feed, making the process suitable for remote operations. SPS of zirconium nitride microspheres has been done before [34], however, the application of SPS to sinter UN microspheres has not been previously studied.

Therefore, the aim of this study was to synthesize homogeneous uranium nitride (UN) and thorium doped uranium nitride [(U,Th)N] microspheres using an aqueous, powder free process, in this case, the internal gelation process. Microspheres were intended to be used directly as feed material for the SPS, and the sintering parameters modified to study their effect in the final pellet density. Furthermore, the effect of thorium in the production, treatment, and properties of the material was also intended to be investigated.

2. Theory

2.1. Internal gelation process

An internal gelation process (IGP) was used to obtain a homogeneous mixture of UO_2, ThO_2 and carbon in the form of microspheres. IGP is based on the hydrolysis and precipitation of metal cations in solution due to the increase in the pH when the solution is heated. The starting nitrate solution is mixed with a complexation agent (Urea) and a gelation agent (HMTA) to produce a sol. Temperature is kept low (0–5 °C) while mixing to prevent the decomplexation and decomposition of the gelation agent [35]. The sol is then dripped into a immiscible heat carrying media to start the gelation. This process has been used previously to produce microspheres of ZrO_2, UO_2, ThO_2, $(U,Pu)O_2$ [30,36,37], all of which can be transformed into carbides or nitrides afterward. The chemistry of the IGP was described by Collins et al. [33] using the following equations:

$$UO_2^{+2}(aq) + 2[CO(NH_2)_2](aq) \leftrightarrow [UO_2 \cdot 2(CO(NH_2)_2)]^{+2}(aq) \quad (5)$$

$$[UO_2 \cdot 2(CO(NH_2)_2)]^{+2}(aq) + 2H_2O \leftrightarrow UO_2(OH)_2(s) + 2(CO(NH_2)_2)(aq) + 2H^+(aq) \quad (6)$$

$$(CH_2)_6N_4(aq) + 4H^+(aq) + 6H_2O \leftrightarrow 4NH_4^+(aq) + 6\,CH_2O\,(aq) \quad (7)$$

In the first step (Eq. (5)) uranyl ions form a complex with urea at low temperatures. The second step (Eq. (6)) involves decomplexation and hydrolysis to form uranyl hydroxide, $[UO_2(OH)_2]$, and hydrogen ions. In the last step (Eq. (7)) the HMTA is decomposed to

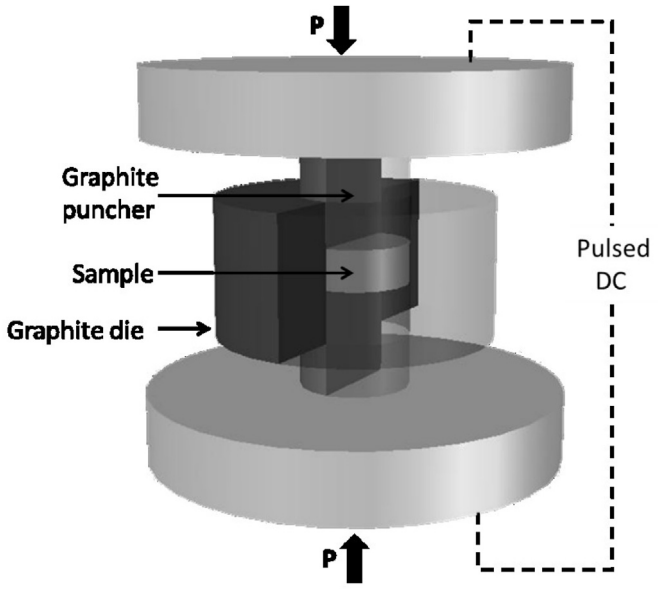

Fig. 1. Graphite die configuration for spark plasma sintering. P indicate the direction of applied pressure.

ammonia and formaldehyde, this reaction removes hydrogen ions from the media, displacing Eq. (6) to the products side.

2.2. Carbothermic reduction

Uranium nitride was then synthesized from microspheres using carbothermic reduction. The process is based on the reaction of UO_2 with carbon to produce uranium carbide under an inert atmosphere. UC can then be transformed into uranium nitride by performing Eq. (9) under a nitrogen atmosphere [19].

$$UO_2(s) + 3C(s) \leftrightarrow UC(s) + 2CO(g) \tag{8}$$

$$2UC(s) + N_2(g) \leftrightarrow 2UN(s) + 2C \tag{9}$$

If uranium dioxide is reacted with carbon under a nitrogen atmosphere, an intermediate uranium carbonitride is observed instead (Eq. (10)) if the temperature is above 1450 °C [38]. Commonly, temperatures between 1500 and 1700 °C are used to carry on Eq. (10)–(12) under an H_2/N_2 atmosphere in order to obtain a fairly pure UN [39].

$$UO_2(s) + (2+x)C(s) + \frac{(1-x)}{2}N_2(g) \leftrightarrow UN_{1-x}C_x(s) + 2CO(g) \tag{10}$$

$$UN_{1-x}C_x(s) + \frac{x}{2}N_2 \leftrightarrow UN(s) + xC \tag{11}$$

$$UO_2(s) + 2C(s) + \frac{1}{2}N_2(g) \leftrightarrow UN(s) + 2CO(g) \tag{12}$$

Further reaction under H_2/N_2 atmosphere and higher temperatures are required to complete the reaction (Eq. (12)) and remove the residual carbon as hydrogen cyanide (HCN) or methane (CH_4), following Eqs (13) and (14) [40,41].

$$2C(s) + N_2(g) + H_2(g) \leftrightarrow 2HCN\,(g) \tag{13}$$

$$C(s) + 2H_2(g) \leftrightarrow CH_4(g) \tag{14}$$

2.3. Spark plasma sintering (SPS)

Sintering is a process involving the fusion of particles by heat or pressure without reaching the melting point, leading to the densification of the material. Spark plasma sintering (SPS), also known as plasma-activated sintering (PAS), is a technique similar to hot pressing, however, an electrical current goes through the graphite punches and the sample, raising the temperature faster and reaching heating rates of up to 1000 °C/min [42–44]. The samples need to be packed in an electrical conductive material, such as graphite, to allow the current to heat the sample. Pressure is applied to the sample at the same time, with the aim of aiding in the densification. It has been shown that SPS allows lower sintering temperatures and times while increasing the densification of different materials, such as alumina [43] or uranium nitride [45]. Fig. 1 presents a schematic representation of the assembly for SPS, where the sample is confined inside the graphite die and the graphite punches are compressed while a current is passed through.

3. Experimental

3.1. Chemicals

Uranyl nitrate hexahydrate (UNH) [$UO_2(NO_3)_2{\cdot}6H_2O$] was prepared inhouse by dissolving metallic uranium (in the form of a metal rod) with conc. HNO_3. The precipitated UNH crystals were filtered and dried in air. Solutions of uranyl nitrate were prepared by dissolving UNH crystals in ultra-pure water (18.2 MΩ cm). Thorium nitrate [$Th(NO_3)_4{\cdot}5H_2O$] was also produced in-house.

Carbon black (MOGUL L) provided by CABOT was used as a carbon source. Hexamethylenetetramine (HMTA) 99% purity was provided by Sigma Aldrich and was used as the gelation agent. Urea in solid form with 99% purity was provided by Sigma Aldrich. Laboratory grade Triton X-100 was received from Sigma Aldrich and was used as a non-ionic surfactant to disperse the carbon powder in the solution [46]. Ultra-pure water (18.2 MΩ cm) was used for all aqueous dilutions.

Silicone oil v 1000 from Rhodorsil was used as the gelation medium. Petroleum ether from Alfa-Aesar was used to wash the oil from the spheres, while ammonium hydroxide solution 28–30% from Sigma-Aldrich was used to wash the unreacted chemicals and to age the spheres.

3.2. Methods

The experimental work was divided into two parts: the synthesis of thorium-doped UN microspheres and pellet formation using spark plasma sintering (SPS).

3.2.1. Synthesis of UN and (U,Th)N microspheres

Sol-Gel process was performed by slowly dripping a cool solution into a hot oil. Firstly, 10 or 15 mL batches with 1.5 M solutions of $UO_2(NO_3)_2$ were cooled in a double jacketed beaker connected to a water bath at 4 °C. NO_3^-/UO_2^{2+} ratio was kept at 2 to avoid the use of sub-stoichiometric nitric acid or two sources of uranium. Solid urea was added to reach a molar ratio of 1.3 between urea and uranium. After the urea was completely dissolved, HMTA was added slowly to reach a molar ratio of 1.8 with the metal. Triton X-100 was added to reach a concentration of 0.02 g/mL. Once the

mixture was homogeneous, graphite was added to obtain a 2.5 M ratio C/Metal. The sol was then left to completely mix for 10–15 min. The final metal concentration was estimated to be 1.1 M. The parameters and ratios used were found experimentally to produce good quality microspheres.

Thorium was added as a dopant in molar fractions of 0.05, 0.1 or 0.2. $Th(NO_3)_4$ in solid form was dissolved in the uranyl solution to reach the desired molar fraction. Afterward, the urea, HMTA, Triton X-100, and carbon were dissolved using the same method as for undoped UN. Thorium addition increased the final metal concentration up to 1.2 M for materials with high thorium doping.

Solutions were then manually dropped into the gelation medium (70 °C silicon oil), trying to maintain a similar droplet size. The spheres were allowed to form and fall in the 30 cm long column. On average, the process took 2 min per milliliter of solution. Spheres were collected and washed twice for 10 min with petroleum ether to remove the silicone oil. The spheres were then washed in concentrated ammonia solution for 10 min to remove unreacted compounds. Washing with diluted ammonia solution was performed to age the spheres. The last step was to leave the spheres to air dry for one or two days.

The dried material was placed in an alumina crucible and taken into an alumina tube furnace ETF 30–50/18-S with a maximum operating temperature of 1800 °C. Samples were dried at 350 °C for 1 h. To reduce the cracking of the spheres a 3 °C/min heating rate was used. For the remaining steps, heating rates of 10 °C/min were used. The reduction of uranium to UO_2 and organic compounds to carbon was done at 800 °C for 1 h. The sample was cooled and then transferred to a clean alumina boat. The nitridation was then performed in the same furnace at 1550 °C for 4 h, followed by 1 h of decarburization at 1650 °C. The temperature profile for the carbothermic nitridation can be seen in Fig. 2. Heating and dwelling were performed in a mixed atmosphere gas (5% H_2 and 95% N_2) provided by Air Liquide. Both coolings were done in an argon atmosphere, this was more important after nitridation to avoid the formation of U_2N_3.

Surface structure and elemental distribution were examined using a Hitachi TM 3000 tabletop SEM/EDX. Part of the material was ground, and the phases and crystallographic structure of the powders were investigated by X-ray diffraction (XRD) using a BRUKER D2 PHASER XRD which includes monochromatic Cu (λ = 1.54184 Å) radiation source in 2θ range of 20° - 144°, and a lynxeye detector. The operation voltage and current used are, respectively, 30 kV and 10 mA. The lattice parameters were

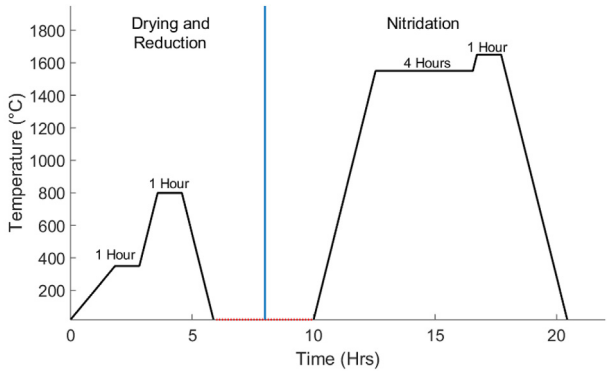

Fig. 2. Temperature profile for carbothermic reduction of uranium nitride. Heatings and reactions were performed under 5% H_2/N_2. Both coolings were performed under an inert atmosphere (Argon). Heating and cooling rates of 10 °C/min were used in all cases.

calculated from the XRD peaks using the following equation [47]:

$$a^2 = \frac{\left(h^2 + k^2 + l^2\right)\lambda^2}{4sin^2(\theta)} \tag{15}$$

Where a denotes the lattice parameter, (hkl) the miller index of the crystallographic plane causing the diffraction peak, λ the wavelength of the X-rays used, and θ the interference diffraction angle.

The elemental composition was determined using a LECO CS744 instrument for carbon, and a LECO TC-436DR for nitrogen and oxygen. A Thermo-Fisher inductively coupled plasma mass spectrometer (ICP-MS) was used to evaluate the thorium/uranium ratio in the materials synthesized.

3.2.2. Pelletizing and sintering

Sintering was performed in a modified DrSinter SPS-5.40 MK-VI machine contained within a glovebox under an inert argon atmosphere. Uranium nitride and doped uranium nitride microspheres were transferred directly into an 8 mm graphite dice. Graphite paper was used to prevent the sample from sticking to the graphite die. The graphite paper was removed afterward by grinding with a silicon carbide (SiC) sandpaper. Sintering in SPS was performed under high vacuum (<10Pa) to avoid damage to the machine. The temperature was increased at a rate of 100 °C/min. Pressure was slowly increased after the temperature reached 400 °C. The sintering temperature was measured on the surface of the graphite die by an optical pyrometer. The temperature was increased to the sintering temperature, where it was held for 10 min, with the exception of one sample where 5 min of isothermal sintering time was used for comparison. Different thorium contents, sintering temperatures, and pressures were used to study the sintering effect on the pellet properties. The sintering parameters are listed in Table 2.

3.2.3. Density measurement

Two density (D) measurement methods were used to establish the efficiency of the sintering process. The average radius and height of the pellet were used to estimate the “geometrical” density and an Accupyc II 1340 gas pycnometer from Micromeritics provided a measurement of the density of the pellet using helium as the analysis gas, thus named “pycnometer” density. For analysis of the surface area and porosity, an ASAP 2020 instrument from Micromeritics was used. This instrument utilizes the BET principle of adsorption and desorption of nitrogen at low temperatures (−196 °C) to obtain information about the surface characteristics of the material.

As materials with different dopant compositions were sintered the innate density of each material was expected to be different. Therefore, the percentage of theoretical density (%TD) was used to compare the procedures instead of their measured density, and this parameter was calculated using the following equation:

$$\%TD = 100 \times \frac{D}{TD} \tag{16}$$

where D is measured density, and TD is theoretical density. The theoretical density can be calculated knowing the crystal structure and composition of the material. For face-centered cubic (FCC) materials, TD can be estimated using Eq. *17*.

$$TD = 4 \times \frac{M_m}{a^3 N_A} \tag{17}$$

where M_m is the molar mass of the compound, a is the lattice parameter and N_A is Avogadro’s constant. Both UN and ThN have an

Table 2
Parameters used in the SPS for the pelletization and sintering of UN and (U,Th)N microspheres. A heating rate of 100 °C/min was used for all samples.

Sample name	Thorium molar composition (%)	Sintering Temperature (°C)	Sintering Pressure (MPa)	Sintering time (min)
UN-1	0	1450	75	10
UN-2	0	1550	75	10
UN-3	0	1650	50	10
UN-4	0	1650	75	5
UN-5	0	1650	75	10
UN-6	0	1650	100	10
UN-7	0	1750	75	10
(U95Th5)N	5	1650	75	10
(U90Th10)N-1	10	1650	75	10
(U90Th10)N-2	10	1750	100	10
(U80Th20)N-1	20	1650	40	10
(U80Th20)N-2	20	1650	75	10

FCC crystal structure, with corresponding lattice parameters of 4.889 Å [16] and 5.160 Å [48]. Evaluation of the position of the peaks on the XRD pattern is an experimental approach used to find the lattice parameter of a mixture of two compounds. Otherwise, it can be estimated theoretically using Vegard's law if the phase composition is known, however, it must be assumed that the phases are pure, and the mixture follows Vegard's law.

3.2.4. Computational simulations

Theoretical simulations were performed in order to understand the variations observed in the sintering process once thorium was introduced. All the calculations were carried out within the density functional theory (DFT) framework using the projected augmented waves (PAW) formalism [49] as implemented in the Vienna ab initio Simulation Package (VASP) [50,51]. Exchange-correlation effects were characterized by the GGA-PBE [52,53]. The potentials were taken from the VASP database, treating 14, 5 and 12 electrons as valence for uranium, nitrogen, and thorium respectively. In order to describe accurately strong correlated f-electrons, the rotationally invariant implementation of Hubbard-U correction, introduced by Liechtenstein et al. was adopted [54]. The on-site Coulomb interaction parameter U and the exchange parameter J were set to 2.0 and 0.1 eV respectively for uranium [55]. The Hubbard-U correction was not applied to thorium because previous studies have successfully modelled ThO_2 [56] and ThN [57] using stranded GGA.

The plane wave cut-off energy was fixed at 600 eV and the fractional electron occupancies were estimated with the method of Methfessel-Paxton, with a smearing width of 0.1 eV. In the present work, we choose a 1k antiferromagnetic structural UN with lattice parameter: a = 5.03 Å, b = 4.97 Å, and c = 4.90 Å as the initial structure according to the previous research [55]. The impurity incorporation energies were calculated based on a 64-atoms supercell, for which the 4 × 4 × 4 Monkhorste-Pack k-point meshes were used. The geometries and ion positions were fully optimized with the force criterion of 0.01 eV/Å, and the total energy was relaxed until the energy difference was smaller than 10-5 eV. The reference states to compute the incorporation and solution energies, namely the chemical potential of N, U, and Th, were chosen as the single-atom energy of nitrogen gas, α-uranium and fcc (cpp)-Cu structural thorium. For the binding energy and migration energy simulations, the reference cell was enlarged to the 216-atoms supercell, in order to avoid the boundary effect. The k-meshes were consequently reduced to 2 × 2 × 2 to keep a constant k-point density. The atomic positions were fully relaxed until the total energy was converged to 10-4 eV and the cell shape and volume were restrained. Migration barriers were calculated using the climbing image nudged elastic band (NEB) method [58,59] with three inter-media images.

4. Results and discussion

4.1. Characterization of UN and (U,Th)N

A series of analyses, such as elemental analysis and XRD measurements, were performed to evaluate the properties of the materials produced. Firstly, the elemental composition was measured. Average values for carbon, nitrogen, and oxygen are listed in Table 3. Carbon and oxygen were present in all samples as impurities. Carbon contents between 0.01 and 2.3 wt-% were measured, and oxygen impurities between 0.08 and 0.6% were found. Uncertainties were estimated by measuring the samples in triplicates. As can be seen in Table 3, there is some variation in relative uncertainties between samples, which can be attributed to the difference in distribution of carbon in each batch of microspheres. It is possible that the temperature used was not high enough to completely remove the free carbon during the hydrogen decarburization, and therefore higher temperatures or longer decarburization times should be necessary to attain lower carbon impurities.

Oxygen is expected to be present in the form of UO_2, as it is most likely the oxygen left due to incomplete reaction in the carbothermic reduction, in addition to oxygen introduced while transporting the sample from the furnace to the glovebox. This is corroborated in the XRD in Fig. 3, where the marked peaks could be attributed to UO_2 phases. Residual carbon is mainly present as carbide, which is dissolved in the nitride phase. In the solid solution, carbon substitutes nitrogen in the crystal structure, causing an increase in the lattice parameter in accordance with Vegard's law. The uranium nitride peaks are thus shifted towards smaller angles.

As previously mentioned, it is expected that thorium and uranium nitrides form a solid solution due to their similar properties, such as crystal structure (FCC) and electronegativity [60]. However, due to thorium's slightly bigger ionic radius compared to uranium, an increase in the lattice parameter is predicted. Therefore, a shift to lower angles is expected in the XRD diffractometer, evidence of which can be seen in Fig. 4. The shifts became more pronounced when a higher amount of thorium was present in the solid solution. The change in the lattice parameter seems to be linear, and therefore it could be possible to estimate the carbon and nitrogen composition in a pure UN sample utilizing Vegard's law. However, once thorium is introduced into the sample the equation becomes unsolvable unless the exact ratio of U/Th is known. Similar results were observed previously by other authors when other dopants, such as chromium, neodymium or plutonium were used [61,62]. The absence of additional peaks indicates that new phases, such as oxides or sesquinitrides, were not formed during the carbothermic reduction.

Surface studies were conducted by scanning electron

Table 3
Elemental characterization of nitride microspheres produced by carbothermic reduction and lattice parameter estimated using the XRD spectra measured. n.d. denotes for not determined. The confidence level for the uncertainties is 2 σ.

Sample name	Thorium molar metal fraction (%)	Nitrogen Content (wt-%)	Carbon Content (wt-%)	Oxygen Content (wt-%)	Lattice Parameters (Å)
UN-1	0	5.2 ± 0.1	0.27 ± 0.01	0.574 ± 0.002	4.896 ± 0.004
UN-2	0	5.0 ± 0.1	0.6 ± 0.1	0.23 ± 0.02	4.896 ± 0.002
UN-3	0	5.4 ± 0.3	0.011 ± 0.004	0.3 ± 0.2	4.891 ± 0.002
UN-4	0	n.d.	2.0 ± 0.1	n.d.	n.d.
UN-5	0	5.3 ± 0.2	0.2 ± 0.1	0.08 ± 0.02	4.894 ± 0.002
UN-6	0	4.02 ± 0.04	2.3 ± 0.4	0.24 ± 0.06	4.92 ± 0.02
UN-7	0	5.3 ± 0.2	0.01 ± 0.03	0.09 ± 0.02	4.892 ± 0.002
(U95Th5)N	5	5.6 ± 0.4	0.010 ± 0.002	0.26 ± 0.02	4.913 ± 0.006
(U90Th10)N-1	10	4.7 ± 0.8	1.1 ± 0.2	0.3 ± 0.1	4.931 ± 0.004
(U90Th10)N-2	10	5.3 ± 0.4	0.3 ± 0.1	0.4 ± 0.1	4.924 ± 0.002
(U80Th20)N-1	20	5.1 ± 0.1	0.5 ± 0.1	0.6 ± 0.1	n.d.
(U80Th20)N-2	20	3.5 ± 0.2	2.4 ± 0.1	0.37 ± 0.02	4.99 ± 0.01

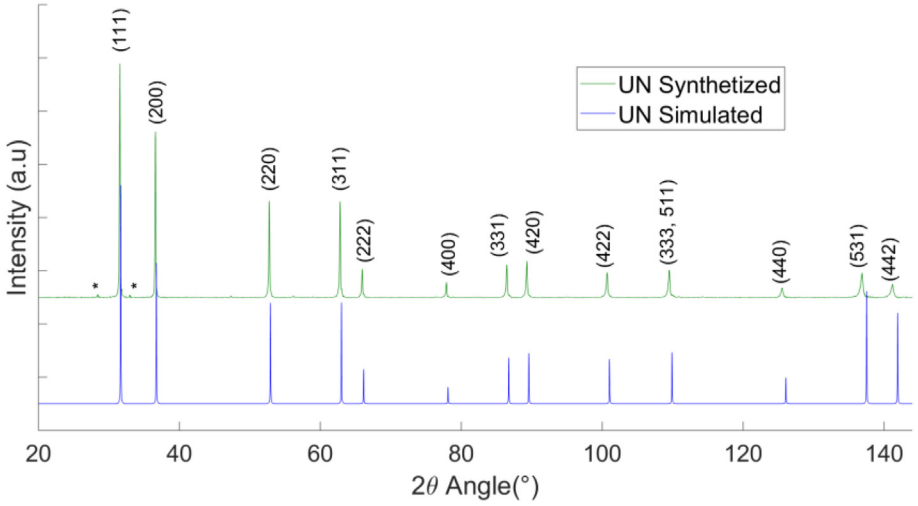

Fig. 3. XRD pattern for a synthetized UN(upper), with an evaluated lattice parameter of 4.894 Å, compared to a simulated XRD pattern for UN (lower), with a lattice parameter of 4.889 Å. * marks the position for possible UO_2 peaks.

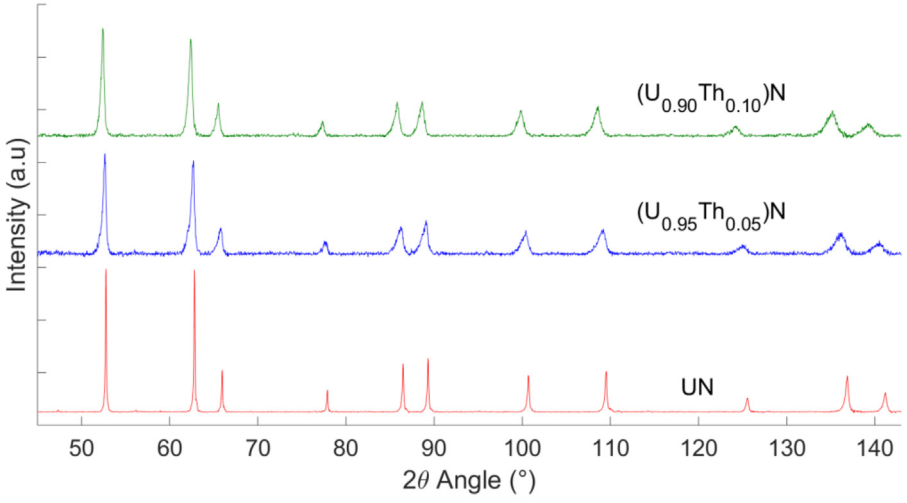

Fig. 4. Effect of thorium composition on the XRD pattern for crushed microspheres synthesized using internal gelation and carbothermic reduction from top to bottom: (U90Th10)N with an estimated lattice parameter of 4.924 Å, (U95Th5)N with a lattice parameter of 4.913 Å and UN with a lattice parameter of 4.894 Å.

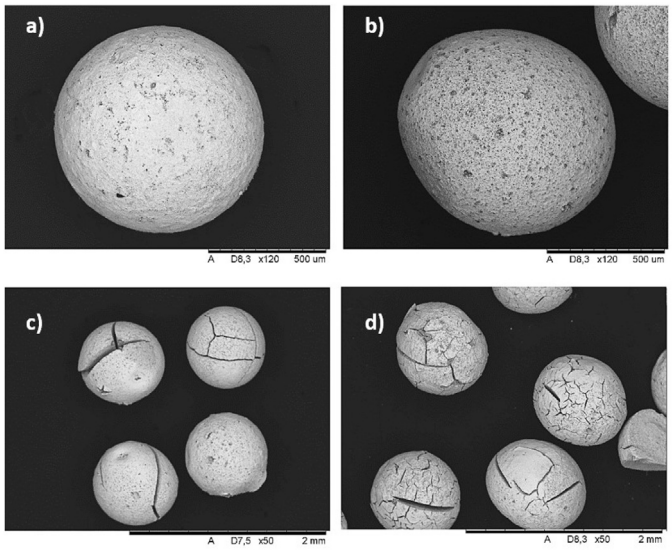

Fig. 5. Scanning electron microscopy of uranium nitride and thorium doped uranium nitride microspheres synthesized using the internal gelation process followed by carbothermic reduction. In order: a) UN, b) (U0.95Th0.05)N, c) (U0.90Th10)N, d) (U0.80Th0.20)N.

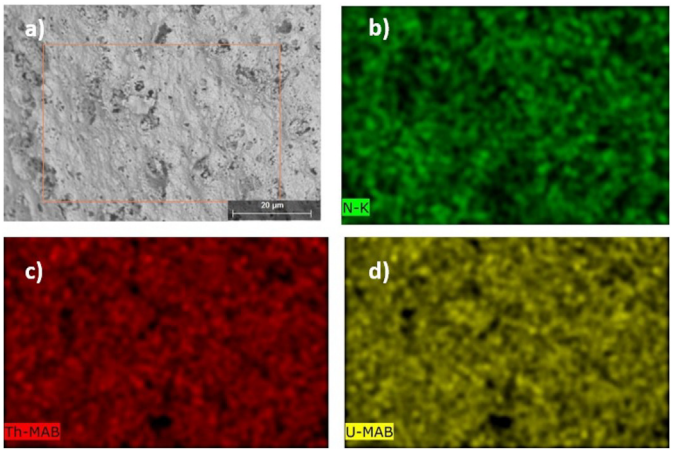

Fig. 6. Elemental distribution in the microsphere surface for a (U0.90Th0.10)N sample synthesized by carbothermic reduction. In order: a) surface SEM (gray), b) nitrogen (green), c) Thorium (red), d) Uranium (yellow). Black zones are imperfections on the surface, such as pores. (For interpretation of the references to colour in this figure legend, the reader is referred to the Web version of this article.)

spectroscopy (SEM/EDX) to determine the structure and elemental distribution in the microspheres. It was observed that the spherical shape was maintained after thermal treatments. However, cracking and high porosity was more notorious at higher thorium concentrations, as seen in Fig. 5. Properties of the microspheres are related to the sol composition used in the gelation process. Once thorium was introduced, the ratio of HMTA had to be increased to be able to precipitate the spheres, as thorium has a higher ionic charge (+4) than the uranyl ion (+2). During the heating process, unwashed reactants increase the gas volume released, which can be the cause of such cracking [63,64].

In addition, using the SEM/EDX it was possible to observe a homogeneous distribution of thorium and nitrogen in the microsphere surface after nitridation, as shown in Fig. 6. However, such distribution might not be entirely correct due to thorium's signal (Lα or Lβ) being similar to uranium in the EDX, which could cause false positives. It is also possible to perceive a high porosity in the surface, which could suggest that the spheres could be easy to crush, and therefore they would be suitable for pelletization.

4.2. Pellet pressing and sintering

Once the material was properly characterized, it was packed, pressed and sintered into pellets. As previously mentioned, the spheres were placed directly in the graphite die and introduced into the SPS machine. Different conditions were used to study the SPS process, and a summary of the parameters is listed in Table 2. The schematic of a sintering curve is shown in Fig. 7. The first increment in displacement is observed when the pressure is increased to the desired value. No apparent shrinking is observed until the onset temperature point is reached, after which it starts increasing until the maximum sintering temperature. Afterward, the displacement rate slows, and by the end of the heat treatment a new plateau is reached.

After the sintering process, the pellets were extracted from the die and the surfaces were polished using the silicon carbide (SiC) sandpaper. Pellets presented a cylindrical shape similar to Fig. 1, with an average 8 mm diameter and 3 mm height. Studies on the pellet surface showed an incomplete removal of the graphite paper, as seen in Fig. 8. It appears that graphite was trapped in the space between the spheres at the surfaces of the pellet, which could affect the density measurements negatively. It was also possible to observe a blackberry structure in the surface, due to spheres not being able to fuse.

Further polishing removed the majority of the graphite, revealing more of the microstructure. It was not possible to observe a resemblance of the blackberry structure in the surface of the pellet after the polishing (Fig. 9a). However, it was possible to observe the presence of a lot of porosity in the bulk of the pellet, better seen in Fig. 9b. This level of porosity could explain the low % TD measured for some of the pellets (Table 4) and can be justified in this particular case by the relatively low pressure used during the sintering process (40 MPa).

Theoretical, geometrical and pycnometer density for UN and thorium-doped UN pellets are listed in Table 4. Densities between 77% and 94% were found for geometrical densities, while pycnometer densities ranged between 88.9 and 98.2%. Geometrical density uncertainties were estimated by measuring the geometrical parameters multiple times. Pycnometer density uncertainties were estimated after measuring the volume with the instrument and the error propagation was performed with respect to the measured uncertainties in both volume and mass.

Big differences in densities between samples are attributed mostly to different sintering parameters used in the process. Difference between the geometrical and pycnometer densities on the same sample can be attributed to the symmetry of the pellet, in addition to the porosity, both closed and open. %TD with pycnometer density provides an estimation of the closed porosity of a pellet, while the geometrical density will additionally include the open porosity and deformation in the geometry. Therefore, the difference between geometrical and pycnometer density should offer an estimation of the open porosity if pellets are symmetrical. Alternatively, if the porosity is known, the pycnometer density could be corrected to include the porosity, therefore resulting in a density measurement that does not suffer from the geometry of the pellet. It is possible to see in Table 4 that, on average, the pycnometer densities decreased by 0.56% after the correction by the porosity volume. These density values are still higher than the geometrical densities, which can imply that the open-pore volume measured represents only a small portion of the total porosity of the pellet. It can also be seen that the uncertainty in the geometrical

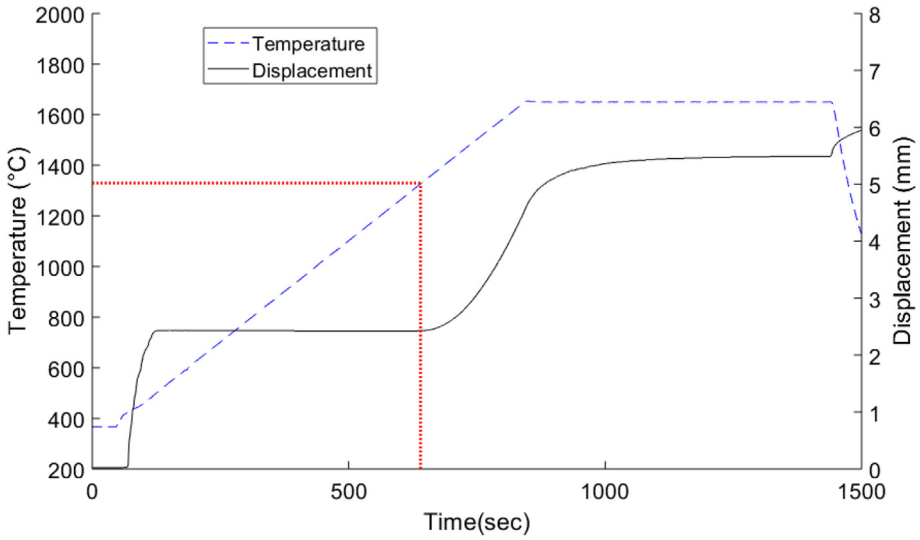

Fig. 7. Sintering profile for sample (U80Th20)N-2. The doted red line indicates the point for onset temperature, found graphically. (For interpretation of the references to colour in this figure legend, the reader is referred to the Web version of this article.)

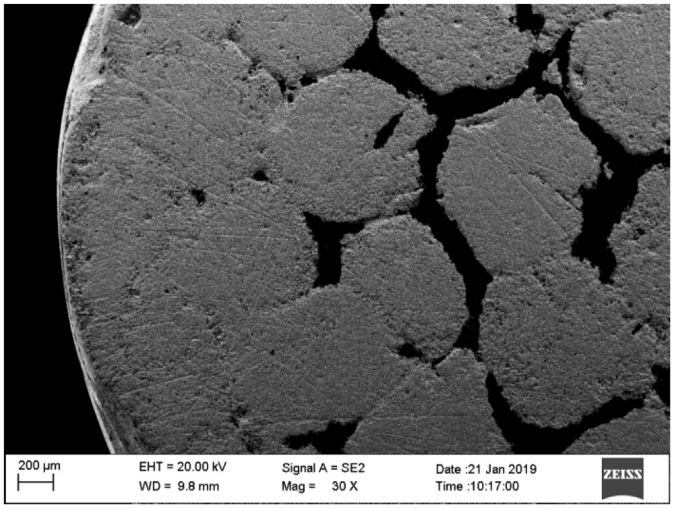

Fig. 8. SEM photograph of the surface of a polished uranium nitride pellet sintered in SPS. Black zones are graphite paper that could not be removed.

measurement is one order of magnitude higher than the pycnometer density, which suggests that the pycnometer density technique is a more precise methodology to measure the density.

The density estimations are comparable with values found elsewhere [29,65]. Nonetheless, pure UN powders are used as feed material instead of mixed nitrides microspheres. There has been previous work on cold pressing and sintering of uranium nitride microspheres [66], however, the densities obtained were lower than 85% TD, which is lower than the results obtained by SPS. Furthermore, the sintering parameters needed were also decreased, for example, the sintering time was decreased from several hours to between 5 and 10 min, which is an advantage if dopants having increased high temperature volatility compared to thorium are used.

4.2.1. Sintering parameters

The temperature effect on sintering followed an expected behavior: the density increased when the temperature was increased. It can be observed in Fig. 10a that both geometrical and pycnometer densities increased, with a more noticeable change in the geometrical density. In Fig. 10b the surface area and pore volume of pellets sintered at different temperatures are presented. As can be seen, at 1550 °C the sintering process reduces the open pore volume and surface area by eliminating most of the open porosity, which increases the pellet density to values between 90 and 95% TD. This, in turn, explains the reduction in the gap between geometric and pycnometric density as sintering temperatures exceeds 1450 °C. The lowest surface area and pore volume were found at

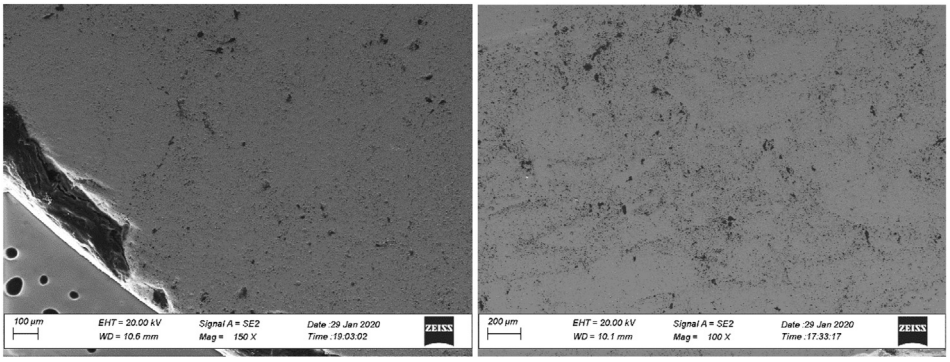

Fig. 9. SEM photograph of (a) the surface of the UN-3 pellet and (b) the cross-section of the (U80Th20)N-1 pellet after polishing.

Table 4
Theoretical densities calculated for UN and (U,Th)N using the lattice parameters determined experimentally with the XRD pattern. Geometrical density was measured using the dimensions of the pellets, while a gas pycnometer was used to measure the pycnometer densities. Pycnometer density was corrected after pore volume measurement. %TD were calculated using Eq. (16). The confidence level for the uncertainties is 2 σ.

Sample name	Theoretical density (g/cm^3)	Geometrical density (g/cm^3)	%TD$_{Geom.}$	Pycnometer density (g/cm^3)	Corrected pycnometer density (g/cm^3)	%TD$_{Pycn.}$
UN-1	14.26 ± 0.04	11.0 ± 0.2	77 ± 4	13.18 ± 0.06	12.91 ± 0.06	90.5 ± 0.5
UN-2	14.26 ± 0.02	12.9 ± 0.6	90 ± 7	13.51 ± 0.06	13.45 ± 0.06	94.3 ± 0.4
UN-3	14.31 ± 0.02	11.5 ± 0.2	80 ± 5	12.81 ± 0.02	12.72 ± 0.02	88.9 ± 0.2
UN-4	14.32[a]	12.2 ± 0.8	85 ± 9	13.3 ± 0.1	13.3 ± 0.1	92.5 ± 0.8
UN-5	14.28 ± 0.02	12.7 ± 0.2	89 ± 5	13.36 ± 0.05	13.30 ± 0.05	93.1 ± 0.4
UN-6	14.0 ± 0.2	12.3 ± 0.2	87 ± 5	12.77 ± 0.05	12.67 ± 0.05	90 ± 1
UN-7	14.30 ± 0.02	13 ± 1	91 ± 11	14.07 ± 0.06	14.05 ± 0.06	98.2 ± 0.4
(U95Th5)N	14.10 ± 0.06	12.8 ± 0.4	91 ± 6	13.51 ± 0.06	13.42 ± 0.06	95.2 ± 0.6
(U90Th10)N-1	13.93 ± 0.04	12.4 ± 0.6	89 ± 7	13.15 ± 0.06	13.10 ± 0.06	94.1 ± 0.5
(U90Th10)N-2	13.99 ± 0.02	13.2 ± 0.4	94 ± 6	13.73 ± 0.08	13.66 ± 0.08	97.7 ± 0.6
(U80Th20)N-1	13.79[a]	10.9 ± 0.2	79 ± 5	12.51 ± 0.03	12.46 ± 0.04	90.4 ± 0.3
(U80Th20)N-2	13.4 ± 0.1	12.1 ± 0.2	90 ± 5	12.80 ± 0.04	12.75 ± 0.04	95.0 ± 0.9

[a] As lattice parameters were not determined for these samples, the TD was estimated using the reported lattice parameters for UN and ThN.

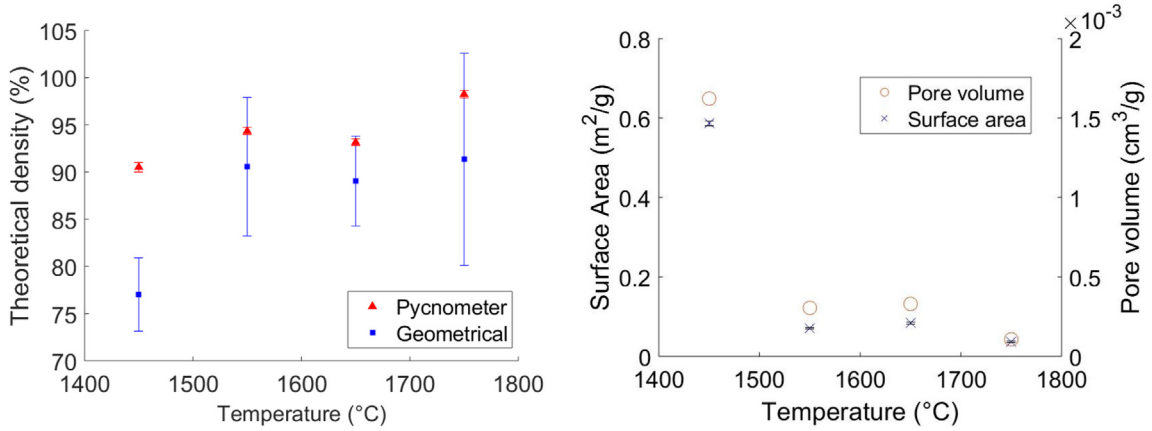

Fig. 10. Final pycnometer(Δ) and geometrical (□) density, surface area(x) and pore volume (○) of UN pellets as a function of the sintering temperature. Sintering pressure and time were maintained constant at 75 MPa and 10 min respectively. The confidence level for the uncertainties is 2 σ.

1750 °C, where the pellet density reached values of 98%TD.

Regarding the effect of pressure in the pelletization process, it is possible to observe a trend of higher densities at higher pressures, as shown in Fig. 11. At pressures lower than 50 MPa the pellets weren't completely compacted, which caused crumbling, chipping and breaking during the polishing. Densities reached a maximum between 90 and 94% TD when 75 MPa of pressure was used. However, at 100 MPa the pore volume and surface area of the material increased, which caused a lower density than expected by the trend. There is no certain explanation for such behavior. Nonetheless, it can be suspected that due to the higher carbon impurity, in the form of both carbide and graphite, the error introduced in the calculation of theoretical density becomes significant.

4.2.2. Thorium content

When comparing the sintering profile curves for all the samples, it was observed that all pure UN samples start to sinter below

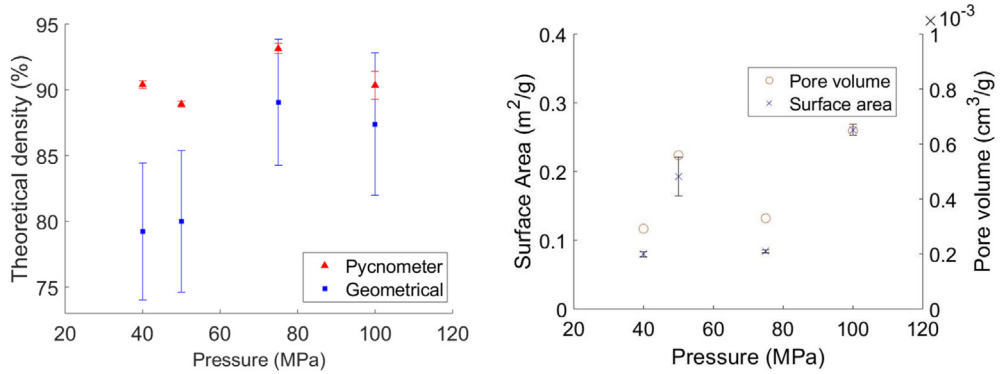

Fig. 11. Final pycnometer(Δ) and geometrical (□) density, surface area(x) and pore volume (○) of UN pellets as a function of the sintering pressure. Sintering temperature and time were maintained constant at 1650 °C and 10 min respectively. The confidence level for the uncertainties is 2 σ.

1000 °C. However, when thorium was present the sintering onset temperature was increased, and the higher the thorium content, the higher the temperature needed to sinter the pellet, as can be seen in Fig. 12.

The sintering temperature is related to several factors, such as particle size, surface state, and melting point [67]. It is common that materials with higher melting points usually require higher temperatures to sinter [68]. However, ThN melting point is similar to UN, 2820 and 2850 °C, respectively. Moreover, sintering and densification processes can be explained by atomic rearrangement in the crystallographic structure as temperature rises [69]. In order to understand the effect shown in Fig. 12 at an atomic level, DFT calculations were employed to predict the self-diffusion behavior of pure and Th-doped UN. The latter was simulated by introducing a single Th atom into the perfect UN lattice and thus the likely doping position of Th in the UN lattice could be identified.

Here, four possible positions for Th were investigated: substitutional sites at U and N sublattice, the center of the Schottky defect and interstitial site. These positions are illustrated in Ref. [70]. The calculated solution energy Esol, incorporation energy Einc and the corresponding defect formation energy Ef are listed in Table 5. Considering that self-diffusion is enabled by the point-defect of U and N in UN, the solubility of the self-interstitial N and U were also calculated. The results indicate that the most energetic favorable position for Th in UN is the uranium substitutional site. Consequently, Th is always located at or migrates to uranium sublattices in the following studies.

Fig. 13 shows the binding energy of Th with the either vacancies or interstitital in UN. In AFM-UN crystal, Th and U vacancy at the first-nearest-neighbor (1NN) position can have the same or an opposite spin. While 2NN are always located at the sites with the same spin orientation and their configuration can be normal or tangential to the spin plane. More explanations about the configurations can be found in Ref. [70]. 1NN clusters possessing positive binding energies are strongly attractive which means Th prefers to migrate towards these defects which impacts their diffusion behaviors. 2NN clusters having negative binding energies are strongly repulsed indicating that Th will migrate away from the vacancies and have limited impact on diffusion behaviors.

The migration barriers for U and N self-diffusion in UN and Th doped UN were calculated and the results are presented in Fig. 14. Th_s and Th_o in Fig. 14b are the migration barriers for Th-vacancy exchange. For the other migration mechanisms in Fig. 14b, Th atom was placed at the 1NN position of U or N defect and the energy barrier is the energy required for this defect to migrate to another

Table 5
Incorporation and solution energies (eV) of Th in UN and the corresponding defect formation energy. Incorporation energies of self-interstitial N and U are also listed. Most stable configurations are in bold font.

Defect	E_f	E_{inc}	E_{sol}
SubU_Th	**3.64**	**−3.28**	**0.36**
SubN_Th	**3.87**	6.72	10.58
Schottky_Th[a]	3.97	−3.09	0.88
inter_Th		10.37	
inter_N		**2.39**	
inter_U		10.64	

[a] Th relaxed to the uranium vacancy position.

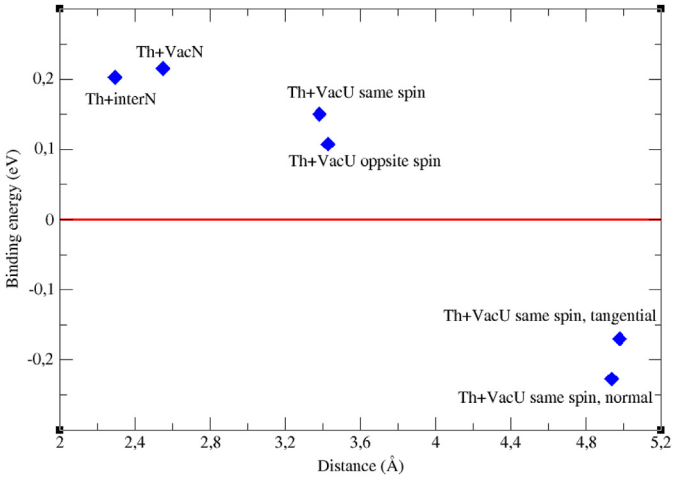

Fig. 13. Binding energy (eV) of Th at uranium substitutional site with the self-point defect in UN. A positive value indicates an attraction, and a negative value indicates a repulsion. The configurations are illustrated in Ref. [12].

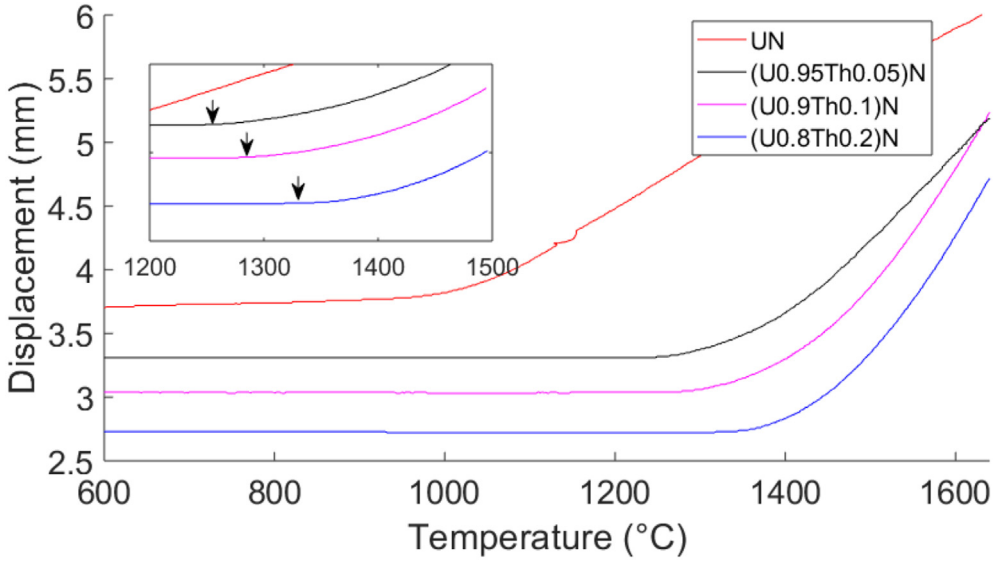

Fig. 12. Sintering profile for different materials when temperature is increased. From top to bottom: UN, (U95Th5)N, (U90Th10)N and (U80Th20)N. Arrows indicate the onset temperature identified graphically, showing the temperature range where the pellet starts to shrink.

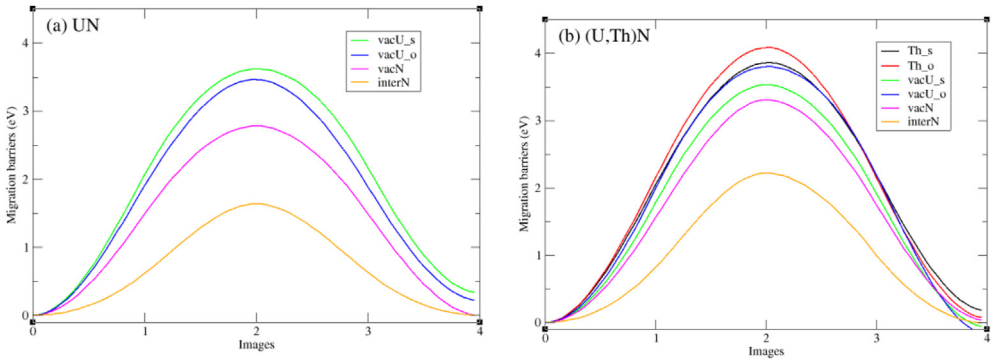

Fig. 14. The migration barriers of the point defects in UN (a) and (U,Th)N (b). s and o mark the U vacancy or Th atom migrating to the same or opposite spin orientation as the initial state, respectively.

1NN position. Comparing the obtained migration barriers shown in Fig. 14a Fig. 14b, it is obvious that the existence of Th significantly increased the migration barriers for the diffusion of N vacancy and interstitial while having a limited impact on the diffusion of U vacancy. It can be concluded from the results that the self-diffusion of Th doped UN is slower than that of pure UN. This conclusion perfectly matched with the experimental observation illustrated in Fig. 12 that doping Th into UN will delay the sintering process.

5. Conclusions

In this work UN and (U,Th)N pellets were prepared by SPS using microspheres as feed material, which has not been reported previously. Thorium was selected due to its reported lower solubility in aqueous systems.

Internal gelation process followed by carbothermic reduction provided a reliable method to manufacture UN and (U,Th)N microspheres. The introduction of thorium caused a change in the gelation process, producing highly cracked microspheres after heating. Therefore, further optimization of the internal gelation process is necessary to reduce the cracking of Th doped microspheres.

Due to their high porosity, and thus low density, these microspheres broke easily and facilitated the pelletization. Thorium nitride formed a homogeneous solid solution with the UN, which was evidenced in the SEM and XRD analysis. No blackberry structure was visible in the bulk of the pellet after polishing, indicating complete microsphere disintegration during pelletization.

Densities measured exceeded 90%, and up to 98%, of TD, which were higher than any other method used before for pelletization. Presence of high porosity was detected in the bulk of the sintered pellet, which could explain the low %TD measured for some samples. It was also observed that temperatures and pressures higher than 1550 °C and 50 MPa, respectively, were necessary to close the majority of the porosity during the sintering process.

It was noticed that the addition of thorium increased the onset temperature for the sintering process. This behavior was attributed to the incorporation of thorium in the uranium sublattice, which raises the migration barrier of defects, as shown in the DFT calculations. Therefore, atomic interdiffusion becomes harder to achieve, increasing the activation energy for that process and thus the temperature required.

Thorium doping showed a reasonable integration in the initial structure of the UN pellets, at the cost of higher temperatures needed for production of sintered materials. In addition, it was also shown that microsphere structure has completely disappear in the bulk after SPS treatment. Further analysis is necessary to fully understand the mechanism of the sintering process.

Declaration of competing interest

The authors declare that they have no known competing financial interests or personal relationships that could have appeared to influence the work reported in this paper.

CRediT authorship contribution statement

L.G. Gonzalez Fonseca: Methodology, Validation, Formal analysis, Investigation, Resources, Data curation, Writing - original draft, Visualization. **M. Hedberg:** Conceptualization, Methodology, Formal analysis, Writing - review & editing, Supervision. **L. Huan:** Software, Formal analysis, Writing - original draft, Visualization. **P. Olsson:** Supervision, Writing - review & editing. **T. Retegan Vollmer:** Supervision, Writing - review & editing.

Acknowledgments

This research was financially supported by the Swedish Foundation for Strategic Research, project number EM16-0031. Huan Liu is financially support by China Scholarship Council (No. 201700260222). The computations were performed on resources provided by the Swedish National Infrastructure for Computing (SNIC) at PDC, KTH. The authors wish to thank the Chalmers Materials Analysis Laboratory (CMAL) for their support during the SEM analysis.

References

[1] H.G. Kim, J.H. Yang, W.J. Kim, Y.H. Koo, Development status of accident-tolerant fuel for light water reactors in Korea, Nucl. Eng. Technol. 48 (2016) 1–15, https://doi.org/10.1016/j.net.2015.11.011.
[2] International Atomic Energy Agency, Accident Tolerant Fuel Concepts for Light Water Reactors, International Atomic Energy Agency, Vienna, 2016.
[3] H.K. Kim, H.G. Kim, J.H. Yang, Y.H. Koo, On the minimum thickness of FeCrAl cladding for accident-tolerant fuel, Nucl. Technol. 198 (2017) 342–346, https://doi.org/10.1080/00295450.2017.1311591.
[4] S.J. Zinkle, K.A. Terrani, J.C. Gehin, L.J. Ott, L.L. Snead, Accident tolerant fuels for LWRs: a perspective, J. Nucl. Mater. 448 (2014) 374–379, https://doi.org/10.1016/j.jnucmat.2013.12.005.
[5] B.J. Jaques, J. Watkins, J.R. Croteau, G.A. Alanko, B. Tyburska-Püschel, M. Meyer, P. Xu, E.J. Lahoda, D.P. Butt, Synthesis and sintering of UN-UO2fuel composites, J. Nucl. Mater. 466 (2015) 745–754, https://doi.org/10.1016/j.jnucmat.2015.06.029.
[6] J.M. Harp, P.A. Lessing, R.E. Hoggan, Uranium silicide pellet fabrication by powder metallurgy for accident tolerant fuel evaluation and irradiation, J. Nucl. Mater. 466 (2015) 1–11, https://doi.org/10.1016/j.jnucmat.2015.06.027.
[7] G.J. Youinou, R.S. Sen, Impact of accident-tolerant fuels and claddings on the overall fuel cycle: a preliminary systems analysis, Nucl. Technol. 188 (2014) 123–138, https://doi.org/10.13182/NT14-22.

[8] K.D. Johnson, A.M. Raftery, D.A. Lopes, J. Wallenius, Fabrication and microstructural analysis of UN-U3Si2composites for accident tolerant fuel applications, J. Nucl. Mater. 477 (2016) 18–23, https://doi.org/10.1016/j.jnucmat.2016.05.004.
[9] Y.S. Kim, Uranium intermetallic fuels (U–Al, U–Si, U–Mo), Compr. Nucl. Mater. (2012) 391–422, https://doi.org/10.1016/B978-0-08-056033-5.00112-9.
[10] K.Y. Spencer, L. Sudderth, R.A. Brito, J.A. Evans, C.S. Hart, A. Hu, A. Jati, K. Stern, S.M. McDeavitt, Sensitivity study for accident tolerant fuels: property comparisons and behavior simulations in a simplified PWR to enable ATF development and design, Nucl. Eng. Des. 309 (2016) 197–212, https://doi.org/10.1016/j.nucengdes.2016.09.009.
[11] R.W. Jones, J.L. Crosthwaite, Atomic energy of Canada limited uranium carbide fuel for organic cooled reactors, 1973.
[12] F.B. Litton, The Properties and Irradiation Behaviour of Carbide Fuels, A Literature Survey, Los Alamos, 1968, https://doi.org/10.2172/4551282.
[13] S.L. Hayes, J.K. Thomas, K.L. Peddicord, Material property correlations for uranium mononitride: III. Transport properties, J. Nucl. Mater. 171 (1990) 289–299, https://doi.org/10.1016/0022-3115(90)90376-X.
[14] J.T. White, A.T. Nelson, J.T. Dunwoody, D.D. Byler, D.J. Safarik, K.J. McClellan, Thermophysical properties of U3Si2 to 1773 K, J. Nucl. Mater. 464 (2015) 275–280, https://doi.org/10.1016/J.JNUCMAT.2015.04.031.
[15] R.M. Dell, V.J. Wheeler, The ignition of uranium mononitride and uranium monocarbide in oxygen, J. Nucl. Mater. 21 (1967) 328–336, https://doi.org/10.1016/0022-3115(67)90185-7.
[16] R.M. Dell, V.J. Wheeler, E.J. Mciver, Oxidation of uranium mononitride and uranium monocarbide*, 1966.
[17] G.A.R. Rao, S.K. Mukerjee, V.N. Vaidya, V. Venugopal, D.D. Sood, Oxidation and hydrolysis kinetic studies on UN, J. Nucl. Mater. 185 (1991) 231–241, https://doi.org/10.1016/0022-3115(91)90340-D.
[18] K. Johnson, V. Ström, J. Wallenius, D.A. Lopes, Oxidation of accident tolerant fuel candidates, J. Nucl. Sci. Technol. 54 (2017) 280–286, https://doi.org/10.1080/00223131.2016.1262297.
[19] B.J. Prewitt, Analysis and Implementation of Accident Tolerant Nuclear Fuels, Missouri University of Science and Technology, 2017.
[20] M. Jolkkonen, P. Malkki, K. Johnson, J. Wallenius, Uranium nitride fuels in superheated steam, J. Nucl. Sci. Technol. 54 (2017) 513–519, https://doi.org/10.1080/00223131.2017.1291372.
[21] Nuclear Power Reactors in the World, International Atomic Energy Agency, Vienna, 2018.
[22] M.P. Brady, I.G. Wright, B. Gleeson, Alloy design strategies for promoting protective oxide-scale formation, J. Occup. Med. 52 (2000) 16–21, https://doi.org/10.1007/s11837-000-0109-x.
[23] A.S. Kuprin, V.A. Belous, V.N. Voyevodin, V.V. Bryk, R.L. Vasilenko, V.D. Ovcharenko, E.N. Reshetnyak, G.N. Tolmachova, P.N. V'Yugov, Vacuum-arc chromium-based coatings for protection of zirconium alloys from the high-temperature oxidation in air, J. Nucl. Mater. 465 (2015) 400–406, https://doi.org/10.1016/j.jnucmat.2015.06.016.
[24] G. Heisbourg, S. Hubert, N. Dacheux, J. Purans, Kinetic and thermodynamic studies of the dissolution of thoria-urania solid solutions, J. Nucl. Mater. 335 (2004) 5–13, https://doi.org/10.1016/j.jnucmat.2004.05.017.
[25] R.B. Malthews, K.M. Chidester, C.W. Hoth, R.E. Mason, R.L. Petty, Fabrication and testing OF uranium nitride fuel for space power reactors, J. Nucl. Mater. 151 (1988) 334–344.
[26] R.R. Metroka, Fabrication of uranium mononitride compacts, NASA Technical Report (1970), NASA-TN-D-5876.
[27] A.A. Bauer, Nitride fuels: properties and potentials, react, Technol. 15 (1972) 87–104.
[28] R. German, Sintering: from Empirical Observations to Scientific Principles, Elsevier Inc., 2014, https://doi.org/10.1016/C2012-0-00717-X.
[29] K.D. Johnson, J. Wallenius, M. Jolkkonen, A. Claisse, Spark plasma sintering and porosity studies of uranium nitride, J. Nucl. Mater. 473 (2016) 13–17, https://doi.org/10.1016/j.jnucmat.2016.01.037.
[30] V.N. Vaidya, Status of sol–gel process for nuclear fuels, J. Sol. Gel Sci. Technol. 46 (2008) 369–381, https://doi.org/10.1007/s10971-008-1725-0.
[31] R.G. Wymer, Laboratory and engineering studies of sol-gel processes at oak ridge national laboratory, accessed May 18, 2018, https://www.osti.gov/servlets/purl/4539651, 1968.
[32] P. Naefe, E. Zimmer, Preparation of uranium Kernels by an external gelation process, Nucl. Technol. 42 (1979) 163–171, https://doi.org/10.13182/NT79-A32147.
[33] B.J. L Collins, M.H. Lloyd, The basic chemistry involved in the internal-gelation method of precipitating uranium as determined by pH measurements*, Radiochim. Acta 42 (1987) 3.
[34] M. Hedberg, M. Cologna, A. Cambriani, J. Somers, C. Ekberg, Zirconium carbonitride pellets by internal sol gel and spark plasma sintering as inert matrix fuel material, J. Nucl. Mater. 479 (2016) 137–144, https://doi.org/10.1016/j.jnucmat.2016.06.034.
[35] J. Collins, M. Lloyd, S. Shell, Control of urania crystallite size by HMTA-urea reactions in the internal gelation process for preparing (U, Pu)O2Fuel Kernels, 2005, https://doi.org/10.2172/885943.
[36] V.N. Vaidya, S.K. Mukherjee, J.K. Joshi, R.V. Kamat, D.D. Sood, A study of chemical parameters of the internal gelation based sol-gel process for uranium dioxide, J. Nucl. Mater. 148 (1987) 324–331, https://doi.org/10.1016/0022-3115(87)90026-2.
[37] M. Streit, Fabrication and Characterisation of (Pu,Zr)N Fuels, ETH Zürich, 2004, https://doi.org/10.3929/ethz-a-004674329.
[38] S.K. Mukerjee, J.V. Dehadraya, V.N. Vaidya, D.D. Sood, Kinetics of the carbothermic synthesis of uranium mononitride microspheres, J. Nucl. Mater. 185 (1991) 39–49, https://doi.org/10.1016/0022-3115(91)90363-C.
[39] T. Muromura, H. Tagawa, Formation of uranium mononitride by the reaction of uranium dioxide with carbon in ammonia and a mixture of hydrogen and nitrogen— I synthesis of high purity UN, J. Nucl. Mater. 71 (1977) 65–72, https://doi.org/10.1016/0022-3115(77)90187-8.
[40] G. Ledergerber, Z. Kopajtic, F. Ingold, R.W. Stratton, Preparation of uranium nitride in the form of microspheres, J. Nucl. Mater. 188 (1992) 28–35, https://doi.org/10.1016/0022-3115(92)90450-Y.
[41] P. Bardelle, D. Warin, Mechanism and kinetics of the uranium-plutonium mononitride synthesis, J. Nucl. Mater. 188 (1992) 36–42, https://doi.org/10.1016/0022-3115(92)90451-P.
[42] M. Omori, Sintering, consolidation, reaction and crystal growth by the spark plasma system (SPS), Mater. Sci. Eng. 287 (2000) 183–188, https://doi.org/10.1016/S0921-5093(00)00773-5.
[43] S.H. Risbud, C.-H. Shan, Fast consolidation of ceramic powders, Mater. Sci. Eng. 204 (1995) 146–151, https://doi.org/10.1016/0921-5093(95)09951-4.
[44] M. Eriksson, Z. Shen, G. Svensson, Policy document for national spark plasma sintering (SPS) facility about SPS access, n.d.
[45] P. Malkki, M. Jolkkonen, T. Hollmer, J. Wallenius, Manufacture of fully dense uranium nitride pellets using hydride derived powders with spark plasma sintering, J. Nucl. Mater. 452 (2014) 548–551, https://doi.org/10.1016/J.JNUCMAT.2014.06.012.
[46] S.M. Fatemi, M. Foroutan, Study of dispersion of carbon nanotubes by Triton X-100 surfactant using molecular dynamics simulation, J. Iran. Chem. Soc. 12 (2015) 1905–1913, https://doi.org/10.1007/s13738-015-0665-1.
[47] E. Smart, Lesley, A. Moore, Elaine, Solid State Chemistry: an Introduction, Third Edit, third ed., Taylor & Francis, 2005.
[48] S. Sugihara, S. Imoto, Hydrolysis of thorium nitrides and carbonitrides, J. Nucl. Sci. Technol. 8 (1971) 630–636, https://doi.org/10.3327/jnst.8.630.
[49] P.E. Blöchl, Projector augmented-wave method, Phys. Rev. B 50 (1994) 17953–17979, https://doi.org/10.1103/PhysRevB.50.17953.
[50] G. Kresse, J. Furthmüller, Efficiency of ab-initio total energy calculations for metals and semiconductors using a plane-wave basis set, Comput. Mater. Sci. 6 (1996) 15–50, https://doi.org/10.1016/0927-0256(96)00008-0.
[51] G. Kresse, J. Hafner, R.J. Needs, Optimized norm-conserving pseudopotentials, J. Phys. Condens. Matter 4 (1992) 7451–7468, https://doi.org/10.1088/0953-8984/4/36/018.
[52] J.P. Perdew, J.A. Chevary, S.H. Vosko, K.A. Jackson, M.R. Pederson, D.J. Singh, C. Fiolhais, Atoms, molecules, solids, and surfaces: applications of the generalized gradient approximation for exchange and correlation, Phys. Rev. B 46 (1992) 6671–6687, https://doi.org/10.1103/PhysRevB.46.6671.
[53] J.P. Perdew, K. Burke, M. Ernzerhof, Generalized gradient approximation made simple, Phys. Rev. Lett. 77 (1996) 3865–3868, https://doi.org/10.1103/PhysRevLett.77.3865.
[54] S. Dudarev, G. Botton, Electron-energy-loss spectra and the structural stability of nickel oxide: an LSDA+U study, Phys. Rev. B Condens. Matter 57 (1998) 1505–1509, https://doi.org/10.1103/PhysRevB.57.1505.
[55] A. Claisse, M. Klipfel, N. Lindbom, M. Freyss, P. Olsson, GGA+U study of uranium mononitride: a comparison of the U-ramping and occupation matrix schemes and incorporation energies of fission products, J. Nucl. Mater. 478 (2016) 119–124, https://doi.org/10.1016/j.jnucmat.2016.06.007.
[56] A.E. Shields, D. Santos-Carballal, N.H. De Leeuw, A density functional theory study of uranium-doped thoria and uranium adatoms on the major surfaces of thorium dioxide, J. Nucl. Mater. 473 (2016) 99–111, https://doi.org/10.1016/j.jnucmat.2016.02.009.
[57] Y. Lu, D.F. Li, B.T. Wang, R.W. Li, P. Zhang, Electronic structures, mechanical and thermodynamic properties of ThN from first-principles calculations, J. Nucl. Mater. 408 (2011) 136–141, https://doi.org/10.1016/j.jnucmat.2010.11.007.
[58] G. Henkelman, B.P. Uberuaga, H. Jónsson, Climbing image nudged elastic band method for finding saddle points and minimum energy paths, J. Chem. Phys. 113 (2000) 9901–9904, https://doi.org/10.1063/1.1329672.
[59] H. Jónsson, G. Mills, K.W. Jacobsen, Nudged elastic band method for finding minimum energy paths of transitions, World Scientific Pub Co Pte Lt, 1998, pp. 385–404, https://doi.org/10.1142/9789812839664_0016.
[60] U. Mizutani, Hume-rothery Rules for Structurally Complex Alloy Phases, CRC Press Inc, 2016.
[61] A. Herman, C. Ekberg, A uranium nitride doped with chromium, nickel or aluminum as an accident tolerant fuel, 2017, p. 5, https://doi.org/10.4172/2321-6212.1000196.
[62] C. Schreinemachers, A.A. Bukaemskiy, M. Klinkenberg, S. Neumeier, G. Modolo, D. Bosbach, Characterization of uranium neodymium oxide microspheres synthesized by internal gelation, Prog. Nucl. Energy 72 (2014) 17–21, https://doi.org/10.1016/j.pnucene.2013.07.016.
[63] R.D. Hunt, F.C. Montgomery, J.L. Collins, Treatment techniques to prevent cracking of amorphous microspheres made by the internal gelation process, J. Nucl. Mater. 405 (2010) 160–164, https://doi.org/10.1016/j.jnucmat.2010.08.007.
[64] W. Tian, M.A. Pouchon, H. Guo, D. Chen, X. Yin, Z. Qin, Fabrication of CeO2 ceramic spheres as a surrogate of nuclear fuel by an improved microwave-assisted rapid internal gelation process, Ceram. Int. 44 (2018) 6739–6746,

https://doi.org/10.1016/j.ceramint.2018.01.090.
[65] H. Muta, K. Kurosaki, M. Uno, S. Yamanaka, Thermal and mechanical properties of uranium nitride prepared by SPS technique, J. Mater. Sci. 43 (2008) 6429–6434, https://doi.org/10.1007/s10853-008-2731-x.
[66] C. Ganguly, R.N. Jayaraj, International Atomic Energy Agency., Indian Nuclear Society., Characterisation and Quality Control of Nuclear Fuels : (CQCNF-2002), Allied Publishers, 2004.
[67] P.S. Liu, G.F. Chen, Making porous metals. Porous Mater, Elsevier, 2014, pp. 21–112, https://doi.org/10.1016/b978-0-12-407788-1.00002-2.
[68] R.H.R. Castro, K. van Benthem, Sintering- mechanism of convention nanodensification and field assisted process, Springer Berlin Heidelberg, 2013, https://doi.org/10.1007/978-3-642-31009-6.
[69] S.J. Kang, Sintering, Elsevier Ltd, 2005, https://doi.org/10.1016/B978-0-7506-6385-4.X5000-6.
[70] A. Claisse, T. Schuler, D.A. Lopes, P. Olsson, Transport properties in dilute UN(X) solid solutions (X=Xe, Kr), Phys. Rev. B 94 (2016), https://doi.org/10.1103/PhysRevB.94.174302.